$J_{X-X})]^2$}. We then expect the singlet lifetime lengthening to be on the order of $[(J_{A-A} - J_{X-X})/(J - J')]^2$. However, the importance of disconnected eigenstates was apparently not appreciated, in part because, in the absence of hyperpolarization and a mechanism to populate the state, the associated state has no obvious applications.

The perturbation calculation is easily extended to diacetyl, where the ratio $(J \pm J')/(J_{A-A} - J_{X-X})$ is also small (the minus sign gives the larger value in cases such as ours, where the couplings have opposite signs). Although the spectra in Fig. 4, C and F, are quite complex, assuming the couplings have the same value as in the hydrate (which gives the excellent spectral fit in Fig. 4F) shows that the overlap of the singlet state with an eigenstate is better than 0.96. This result is also readily verified by precise numerical analysis of this eight-spin system, and thus we predict more than an order-of-magnitude lengthening of the spin lifetime. In effect, the strong coupling between the two carbons quenches communication with other spins—virtually all the spectral complexity comes from the other three carbon states, and singlet-to-triplet interconversion is slow. Of course, perdeuteration dramatically reduces even this limited singlet-triplet mixing and further increases the lifetime.

The advantage of the perturbation theory calculation is that it lets us discuss the generic case. The generalization is more subtle than one might expect. The common case of magnetic equivalence [where the two spins have the same resonance frequency and each of the two spins is coupled identically to every other spin (12)] does not necessarily produce a disconnected eigenstate. For example, any two of the spins in a freely rotating methyl group are magnetically equivalent, but the energy level diagram for three equivalent spins produces no fully disconnected states, so the immunity to environmental perturbations is not present. The only possible disconnected eigenstate for two spins is the singlet; for a larger even number of spins with enough symmetry [e.g., benzene (29)] other disconnected states exist, although they might be difficult to access in practice.

The critical constraint for producing a disconnected eigenstate is that the coupling between two spins substantially exceeds both the couplings to other spins and the resonance frequency difference between the spins. Systems of interest as hyperpolarized contrast agents have two nearby H, ^{13}C, ^{15}N, ^{19}F, or ^{31}P atoms that satisfy this constraint. They have a precursor where the two atoms are inequivalent (hence permitting hyperpolarization of the $\alpha_1\beta_2$ population), which can be converted to the contrast agent by chemical manipulation in a time that is short compared with the normal T_1. Finally, they have a biological pathway that again makes them inequivalent, permitting detection of the hyperpolarization. Diacetyl in vivo satisfies these conditions. Partition in vivo between hydrophobic and hydrophilic phases would modulate the exchange rate (drastically reducing the water concentration and, hence, lengthening the time to convert from singlet); even ignoring hydration, the first

metabolite is acetoin with inequivalent carbons. More generally, the simplest case is two equivalent adjacent carbons or nitrogens without directly bonded hydrogens, as in diacetyl, naphthalene, and oxolin (an antiviral compound) or in many derivatives of pyridazine or phthalazine, which have recently been shown to have vascular endothelial growth factor receptor–2 inhibitory activity (30). In other cases, deuteration can essentially eliminate the coupling to outside nuclei, as could very weak irradiation (far less than is necessary when the spin systems differ in their chemical shift frequency). At moderate fields, even molecules with not-quite-equivalent spins (such as the 3,4-^{13}C versions of L-dopa or dopamine) might be usable, as the degradation pathway leads to compounds such as HVA with substantial asymmetry.

References and Notes

1. J. R. MacFall et al., Radiology 200, 553 (1996).
2. C. R. Bowers, D. P. Weitekamp, J. Am. Chem. Soc. 109, 5541 (1987).
3. J. Natterer, J. Bargon, 31, 293 (1997).
4. K. Golman et al., Magn. Reson. Med. 46, 1 (2001).
5. A. Abragam, M. Goldman, Rep. Prog. Phys. 41, 395 (1978).
6. K. Golman, J. H. Ardenkjaer-Larsen, J. S. Petersson, S. Mansson, I. Leunbach, Proc. Natl. Acad. Sci. U.S.A. 100, 10435 (2003).
7. D. A. Hall et al., Science 276, 930 (1997).
8. J. Kurhanewicz, R. Bok, S. J. Nelson, D. B. Vigneron, J. Nucl. Med. 49, 341 (2008).
9. K. Golman et al., Cancer Res. 66, 10855 (2006).
10. M. E. Merritt et al., Proc. Natl. Acad. Sci. U.S.A. 104, 19773 (2007).
11. I. J. Day, J. C. Mitchell, M. J. Snowden, A. L. Davis, Magn. Reson. Chem. 45, 1018 (2007).
12. C. Gabellieri et al., J. Am. Chem. Soc. 130, 4598 (2008).
13. E. R. McCarney, B. L. Armstrong, M. D. Lingwood, S. Han, Proc. Natl. Acad. Sci. U.S.A. 104, 1754 (2007).
14. The nomenclature used here is explained more fully, with specific examples, in textbooks such as (15).
15. E. D. Becker, High Resolution NMR: Theory and Chemical Applications (Academic, San Diego, 2000), pp. 171–175.
16. M. Carravetta, O. G. Johannessen, M. H. Levitt, Phys. Rev. Lett. 92, 153003 (2004).
17. M. Carravetta, M. H. Levitt, J. Chem. Phys. 122, 214505 (2005).
18. P. Ahuja, R. Sarkar, P. R. Vasos, G. Bodenhausen, J. Chem. Phys. 127, 134112 (2007).
19. G. del Campo, M. C. Carmen Lajo, Analyst (London) 117, 1343 (1992).
20. See http://seattlepi.nwsource.com/dayart/20071221/DiacetylProducts2.pdf for a study done by the Seattle Post-Intelligencer in December 2007.
21. F. G. B. G. J. van Rooy, Am. J. Respir. Crit. Care Med. 176, 498 (2007).
22. R. P. Bell, Adv. Phys. Org. Chem. 4, 1 (1966) and references therein.
23. W. H. Hoecker, B. W. Hammer, J. Dairy Sci. 25, 175 (1942).
24. J. Å. Jakobsen et al., Eur. Radiol. 15, 941 (2005).
25. R. J. Abraham, H. J. Bernstein, Can. J. Chem. 39, 216 (1961).
26. F. A. L. Anet, Can. J. Chem. 39, 2262 (1961).
27. J. I. Musher, E. J. Corey, Tetrahedron 18, 791 (1962).
28. J. A. Pople, W. G. Schneider, H. J. Bernstein, Can. J. Chem. 35, 1060 (1957).
29. A. Saupe, Z. Naturforsch. 20a, 572 (1965).
30. A. S. Kiselyov, V. V. Semenov, D. Milligan, Chem. Biol. Drug Des. 68, 308 (2006).
31. This work was supported by the NIH under grant EB02122 and by the North Carolina Biotechnology Center. We thank D. Bhattacharyya for his help in determining optimal conditions to hyperpolarize diacetyl; M. Jenista for help with calculations; T. Ribiero for his assistance in running NMR spectra; L. Bouchard for discussions of singlet character in strongly coupled systems; and S. Craig, E. Toone, D. Coltart, and M. S. Warren for particularly useful discussions on the chemistry of these compounds. A provisional patent has been submitted on this work by W.S.W. and Duke University.

Greatly Expanded Tropical Warm Pool and Weakened Hadley Circulation in the Early Pliocene

Chris M. Brierley,[1]* Alexey V. Fedorov,[1]*† Zhonghui Liu,[2]* Timothy D. Herbert,[3] Kira T. Lawrence,[4] Jonathan P. LaRiviere[5]

The Pliocene warm interval has been difficult to explain. We reconstructed the latitudinal distribution of sea surface temperature around 4 million years ago, during the early Pliocene. Our reconstruction shows that the meridional temperature gradient between the equator and subtropics was greatly reduced, implying a vast poleward expansion of the ocean tropical warm pool. Corroborating evidence indicates that the Pacific temperature contrast between the equator and 32°N has evolved from ~2°C 4 million years ago to ~8°C today. The meridional warm pool expansion evidently had enormous impacts on the Pliocene climate, including a slowdown of the atmospheric Hadley circulation and El Niño–like conditions in the equatorial region. Ultimately, sustaining a climate state with weak tropical sea surface temperature gradients may require additional mechanisms of ocean heat uptake (such as enhanced ocean vertical mixing).

The early Pliocene [~5 to 3 million years ago (Ma)] is often considered the closest analog to the effects of contemporary global warming on Earth's climate. Indeed, the external factors that control the climate system—the intensity of sunlight incident on Earth's surface,

global geography (1, 2), and, most important, the atmospheric concentration of CO_2 (3)—were similar to present-day conditions. However, high latitudes were warmer, continental ice sheets were largely absent from the Northern Hemisphere, and the sea level was ~25 m higher than today (4, 5).

The climate of the tropics was also quite different. The sea surface temperature (SST) contrast between the eastern and western equatorial Pacific was very small, and cold surface waters were almost absent from coastal upwelling zones off the western coasts of Africa and the Americas (6–10). These climate conditions are often called a "permanent El Niño" or permanent El Niño–like state (11). This term describes the long-term mean state of the ocean-atmosphere system. In contrast, the modern, intermittent El Niño is the warm phase of a quasi-periodic climate oscillation, which affects weather and climate patterns worldwide every 4 to 5 years (12, 13). Interannual climate variability may have also existed in the Pliocene (14), but only during times when the equatorial SST gradient exceeded some critical value (12).

This study focuses on the meridional distribution of SST and its effects on the early Pliocene climate. Understanding changes in this distribution, including variations in the meridional extent of the ocean tropical warm pool, is essential for understanding mechanisms responsible for the gradual transition from the warmer Pliocene to the cooler Pleistocene. It has been hypothesized that the early Pliocene had a relatively deep ocean thermocline in the tropics and that the subsequent shoaling of the thermocline signaled the transition to a colder climate (6). A reduced meridional gradient is required to sustain a deeper tropical thermocline (see below).

We first examined the evolution of the meridional SST gradient over the past 4 million years in the eastern tropical Pacific (Fig. 1, A and C). We used orbitally resolved records from two Ocean Drilling Program (ODP) sites: Site 1012 (32°N, 118°W) from the California margin, and Site 846 (3°S, 91°W) from the eastern Pacific cold tongue just south of the equator (Fig. 1B). Both data sets are based on alkenone-derived estimates of SST (15). The new data from ODP Site 1012 agree overall with previously published results from ODP Site 1014 (8); however, the present data set has much higher resolution, allowing precise temporal alignment of equatorial and subtropical records.

According to these data, the mean temperature contrast between the two sites evolved from a very small value of ~2°C at 4 Ma to 7°C by 2 Ma, and then remained fairly constant at nearly present-day levels (Fig. 1C). Superimposed on the gradual trends at each site are Milankovitch cycles driven by variations in Earth's orbital parameters (1). On orbital time scales, these cycles can produce changes in the SST contrast between the two sites as large as the underlying long-term trends.

The temporal development of the zonal SST gradient along the equator (7) generally mirrors that of the meridional SST gradient in the eastern Pacific (Fig. 1D), suggesting a strong link between extratropical and tropical ocean conditions. The zonal SST gradient reaching its modern value later in the record indicates that meridional temperature changes precondition zonal changes along the equator.

To show that the strong reduction in the meridional temperature gradient in the early Pliocene is a robust result, we reconstructed the meridional SST distribution in the mid-Pacific roughly along the dateline (Fig. 2). The period of this reconstruction is ~4 to 4.2 Ma, sometimes called the Pliocene thermal optimum (16). This period coincides with an almost complete collapse of the east-west temperature gradient along the equator (6–8) (Fig. 1D); it also follows the closure of the Central America Seaway (2) but precedes climate cooling and the development of large Northern Hemisphere ice sheets (1).

The data in Fig. 2 are based on alkenone and Mg/Ca temperature proxies. Alkenone-derived records for ODP Sites 982, 1012, and 1090 and for Deep Sea Drilling Project Site 607 were produced specifically for this study; the original temperature records for other sites were published elsewhere (6–10, 17–21). Adjustments were applied to some of the SST data to represent the mid-Pacific in the early Pliocene (15). For example, when using temperatures from the Atlantic to reconstruct Pacific SSTs, one must consider that temperatures in the North Atlantic are typically 2° to 7°C higher than in the North Pacific; when using SSTs from the eastern boundary of the basin to reconstruct temperatures in the mid-Pacific, one should correct for the effect of coastal upwelling. The overall temperature distribution in Fig. 2 is robust and does not depend on any individual data point.

Our analysis indicates a considerably warmer Pacific climate in the early Pliocene than that determined by the PRISM project in its mid-Pliocene SST reconstructions (5, 22, 23). Furthermore, a strong reduction in the SST gradient from the equator to the subtropics described in our study implies a vast poleward expansion of the ocean low-latitude warm pool (fig. S1), whereas the maximum tropical temperatures remained close to present-day values (28° to 29°C).
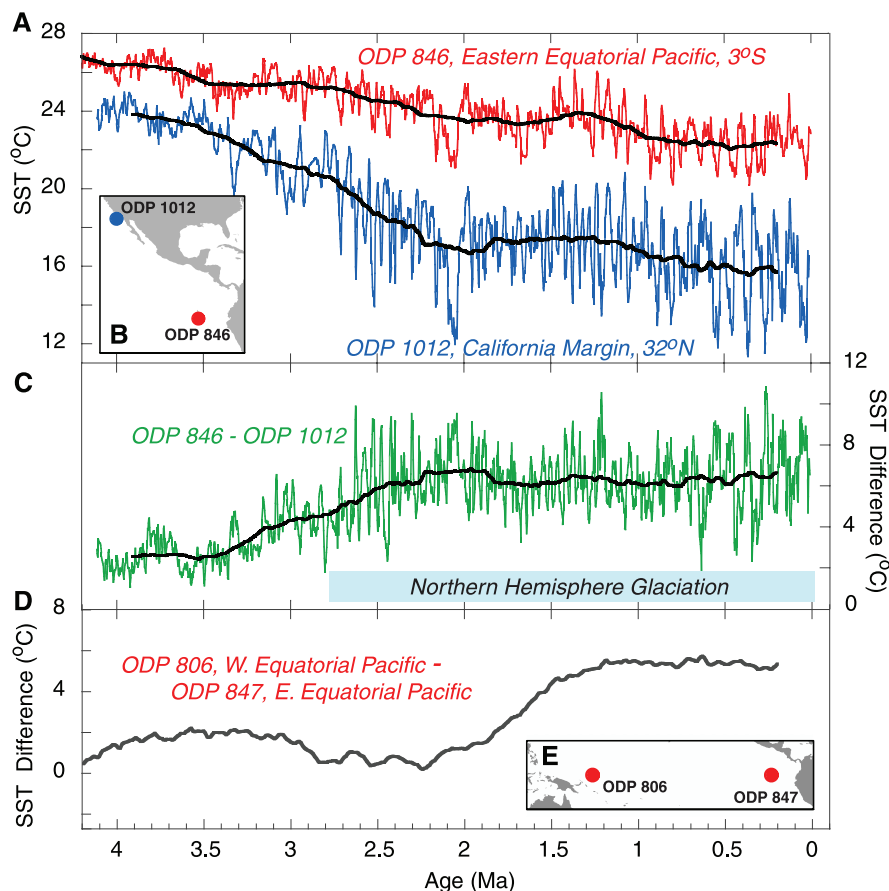
Fig. 1. (**A**) The evolution of SSTs, as derived from alkenones (15), in two locations: ODP Site 1012 (blue) off the coast of California (32°N, 118°W) and ODP Site 846 (red) in the eastern Pacific just south of the equator (3°S, 91°W). Note the cooling trends over the past 4 million years, shown here as 400,000-year running means (black lines). (**B**) Locations of the sites in (A). (**C**) SST difference between the two locations in (B). The meridional SST gradient is minimal at ~4 Ma (2°C) and then increases gradually to modern values (~7.5°C). (**D**) The zonal SST gradient along the equator (7) from Mg/Ca paleothermometry between ODP Site 806 in the western equatorial Pacific (0°N, 159°E) and ODP Site 847 in the eastern equatorial Pacific (0°N, 95°W). The strength of this temperature gradient varies from 0° to 2°C between 5 Ma and 2 Ma and then increases gradually to modern values (~5.5°C). (**E**) Locations of the sites in (D).

[1]Department of Geology and Geophysics, Yale University, New Haven, CT 06520, USA. [2]Department of Earth Sciences, University of Hong Kong, Hong Kong, PRC. [3]Department of Geological Sciences, Brown University, Providence, RI 02912, USA. [4]Geology and Environmental Geosciences, Lafayette College, Easton, PA 18042, USA. [5]Ocean Sciences, University of California, Santa Cruz, CA 95064, USA.

*These authors contributed equally to this work.
†To whom correspondence should be addressed. E-mail: alexey.fedorov@yale.edu

The ocean tropical warm pool (currently confined mainly to the western equatorial Pacific) is a critical component of the climate system (*24*), and changes in its meridional extent can have large implications for climate. In particular, meridional expansion of the warm pool provides a crucial mechanism for maintaining permanent El Niño conditions in the equatorial region, because cold water in the modern eastern equatorial Pacific is sourced from the subtropical subduction zones. Poleward expansion of the warm pool into the subduction regions would lead to warmer waters upwelling in the eastern equatorial Pacific, a deeper ocean thermocline, and consequently a substantial reduction of the SST gradient along the equator. Apparently, such a climate state prevailed at ~4 Ma (Fig. 1, C and D). Thus, to explain the permanent El Niño conditions during the early Pliocene, it is necessary to understand the meridional expansion of the ocean warm pool.

To quantify the atmospheric response to the expanded tropical warm pool and reduced meridional temperature gradient, we fit a hypothetical SST profile to the data in Fig. 2, which was then used as a boundary condition for an atmospheric general circulation model (GCM) (*15*). In the absence of reliable simulations of the Pliocene climate with coupled models, simulations with atmospheric GCMs forced with ocean surface boundary conditions arguably remain the best way to assess climate conditions. Previous studies of the Pliocene with atmospheric GCMs used either earlier PRISM SST reconstructions (*5*), which lacked adequate data for the tropics and subtropics, or the modern SST profile taken from the dateline and extended zonally (*25*).

Our numerical calculations confirm that the SST changes in Fig. 2 strongly affect the global climate and atmospheric circulation. As expected, the lack of an SST gradient along the equator acts to eliminate the atmospheric zonal circulation [the Walker cell (*13*)] (fig. S2). However, if the meridional SST gradient were kept at present-day values as in previous studies, the atmospheric meridional circulation [the Hadley cells (*26*)] would compensate by strengthening substantially (*25*). In contrast, in calculations using our Pliocene SST reconstruction, the Hadley circulation weakens (Fig. 3, A and B).

The Northern Hemisphere branch of the Hadley circulation weakens on average by roughly 30%. During boreal winter, the reduction reaches nearly 40%. The center of the Hadley cell moves northward by ~7°, whereas the cell's latitudinal extent (*26*) increases by 3° to 4°. These changes of the Northern Hemisphere circulation are a robust response to changes in meridional SST gradient as evinced by additional sensitivity calculations (table S2). The volume transport of the circulation's southern branch nearly halves, making the southern Hadley cell even weaker than the northern cell. Whether this is a genuine feature of the early Pliocene climate remains to be seen, because there are only a few SST data points currently available in the Southern Hemisphere. Note that coupled models simulating global warming also show a weakening and poleward expansion of the Hadley circulation. However, those effects

are rather modest—roughly 4% and 1° of latitude, respectively, by the end of the 21st century (*26*).

In our calculations, the reduced meridional temperature gradient also widens the Intertropical Convergence Zone [ITCZ (*13*)] and decreases its

precipitation intensity (Fig. 3, C and D). A second, weaker ITCZ develops in the Southern Hemisphere, caused by the use of a completely symmetrical SST profile. The spatial structure of Pliocene precipitation indicates that the strongest air uplift occurs over

Fig. 2. Estimated distribution of SST with latitude in the middle of the Pacific (roughly along the dateline) at ~4 Ma. This temperature reconstruction uses data from the Pacific and Indian oceans (red boxes) and adjusted data from the Atlantic (blue boxes). Open boxes indicate alkenone-based data; solid boxes indicate Mg/Ca-based data. Thin solid line: SST from the dateline for the modern climate. Dashed line: latest estimates of the mid-Pliocene temperatures (~3 Ma) along the dateline from the PRISM project (*22*, *23*). Thick gray line: a portion of the hypothetical SST profile used as a boundary condition for numerical simulations. The original data and the temperature adjustments are given in table S1.
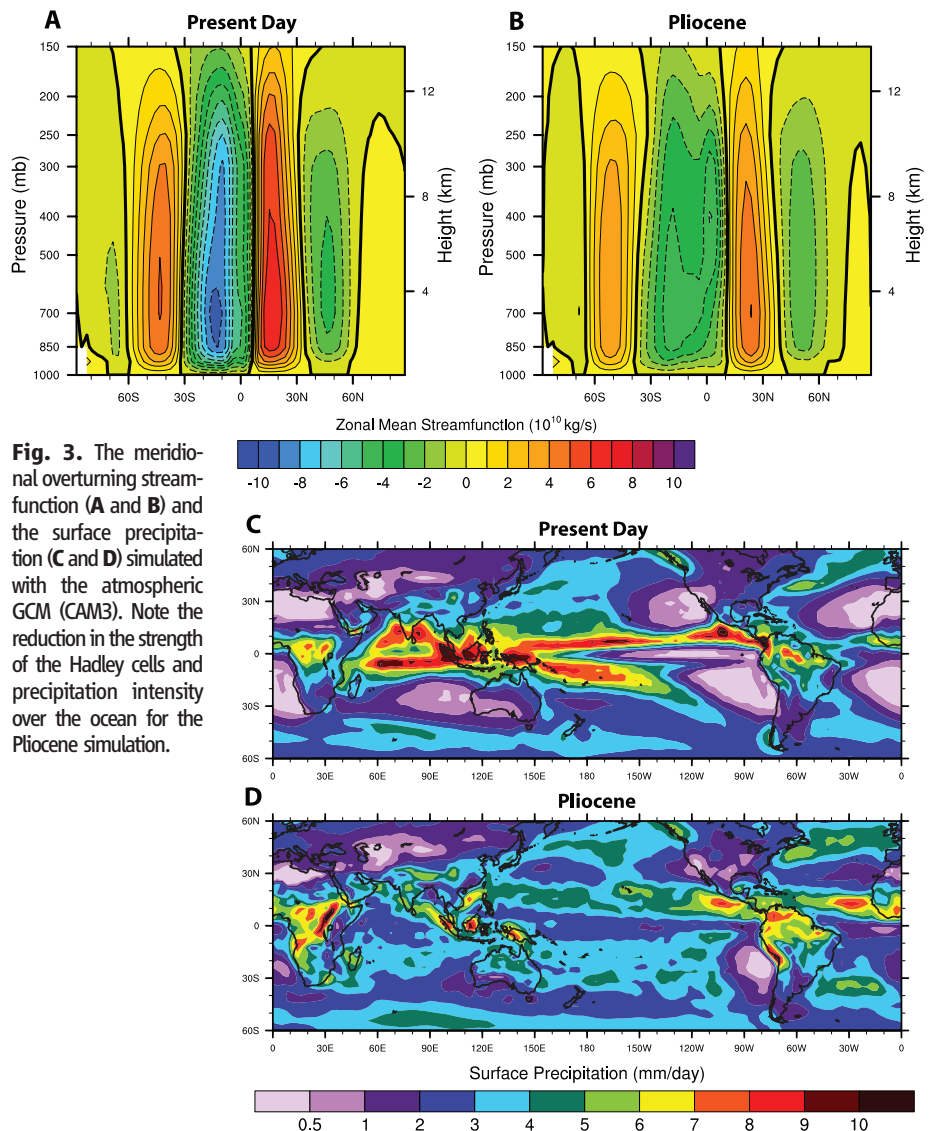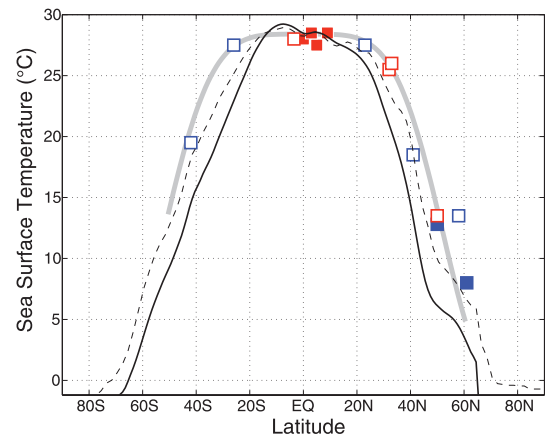

Fig. 3. The meridional overturning streamfunction (**A** and **B**) and the surface precipitation (**C** and **D**) simulated with the atmospheric GCM (CAM3). Note the reduction in the strength of the Hadley cells and precipitation intensity over the ocean for the Pliocene simulation.
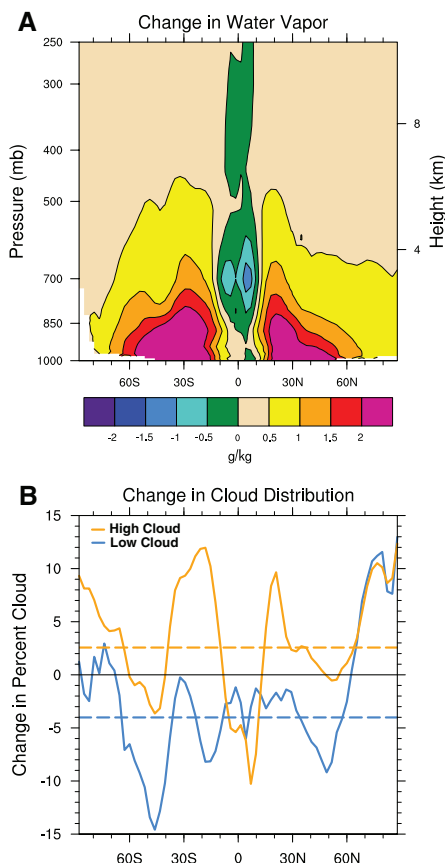
Fig. 4. Factors critical for maintaining a warm Pliocene climate. (**A**) The increase in zonal-mean specific humidity (or water vapor content) from the present day to the early Pliocene (in g/kg). The only reduction in water vapor occurs in a narrow region above the modern ITCZ location, which indicates a weakening of the deep convection in the tropics. (**B**) Changes in cloud distribution with latitude (solid lines) and their globally averaged values (dashed lines). There is a net increase in cloud fraction for "greenhouse" high clouds and a net decrease for highly reflective low clouds; both effects tend to warm Earth's surface.

Fig. 5. Difference in ocean temperatures (averaged over the top 250 m) between two greenhouse-warming simulations: a simulation for which we increased the background vertical diffusivity in the upper 400 m of the ocean by an order of magnitude between 40°N and 40°S, and a control simulation. In each case, the CO_2 concentration was increased instantaneously from preindustrial levels to 355 ppm, and the coupled model (CCSM3) has been integrated for 180 years (the plot is obtained from a 30-year average at the end of the simulations). A gradual ocean adjustment will continue after 180 years, but we do not expect large qualitative changes in the warming pattern. The actual values of the ocean vertical diffusivity in the Pliocene are highly uncertain, so these experiments serve only to demonstrate the proposed mechanism.

orographic features (such as the East African Highlands) rather than over the ocean. Weak SST gradients, and hence a lack of localized wind convergence, over the ocean cause orographic air uplift and ocean-land temperature contrasts to become essential for triggering tropical precipitation.

Terrestrial paleodata provide verification of gross changes in precipitation anticipated over land by our calculations. For example, the model predicts stronger precipitation over southwest and east Africa, the Sahara desert, and Australia, consistent with pollen-based precipitation data (table S3). Comparison of changes over North America is inconclusive because of large error bars in the paleodata (27) and large natural variability in precipitation intensity in that region.

The water vapor content of the atmosphere increases significantly (Fig. 4A) as a consequence of the Clausius-Clapeyron relationship (28), despite the substantial reduction in the strength of atmo-
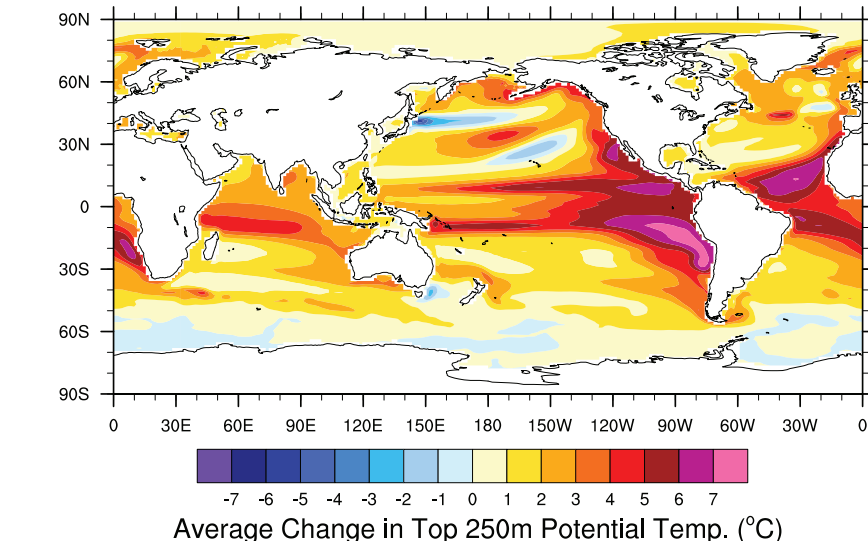
spheric convection over the ITCZ in the Pacific. The increase in water vapor (a potent greenhouse gas) is a major factor in sustaining the warm Pliocene climate. It causes a reduction of 14.6 W m^{-2} in outgoing long-wave radiation at the top of the atmosphere (relative to the present); variations in cloud distribution (Fig. 4B) account for a further reduction of 5.6 W m^{-2}. Because the net increase in atmospheric water vapor (by roughly 30%) is largely a consequence of the expanded ocean warm pool, a climate model will not be able to capture the full extent of the Pliocene warmth unless it can simulate SST patterns in the tropics and subtropics correctly.

Further, our calculations show a slight increase in total poleward heat transport from low to high latitudes (fig. S3). However, the partitioning of the heat transport between the ocean and atmosphere poses the following problem: We find a significant decrease in the heat transport by the atmosphere and an implied increase in ocean heat transport (fig. S3). This result contradicts studies using ocean GCMs with low vertical diffusion, which suggest that a permanent El Niño should be associated with reduced heat transport by the ocean (29). According to those studies, the ocean typically gains a large amount of heat over the tropical Pacific cold tongue; warmer conditions in that region would entail a reduction in ocean heat uptake there, and hence a smaller ocean heat transport. Attempts to simulate the Pliocene climate with coupled atmosphere-ocean GCMs (14) have not yet succeeded in replicating the collapse of the SST gradient along the equator, presumably because of this issue.

One way to resolve the heat transport problem in such a climate state with weak SST gradients is to allow the ocean to gain heat over a much broader

region of the tropics than just the equatorial cold tongue. This would necessitate a substantial increase in ocean vertical mixing rates (or vertical diffusion), which may result from weaker ocean stratification (20) and/or enhanced mixing of the upper ocean by hurricanes (30). Should such an increase in ocean mixing occur, it would lead to larger heat uptake and greater poleward heat transport by the ocean, even with a weak or absent equatorial cold tongue.

To test this hypothesis, we ran a coupled GCM with elevated atmospheric CO_2 concentrations and vertical diffusion uniformly increased in the upper tropical ocean. Preliminary results with enhanced mixing produce a mean state much closer to a permanent El Niño (Fig. 5). There is a much greater warming in the eastern equatorial Pacific than in the west, a warming of the upwelling regions, and a deeper ocean thermocline. At the same time, interannual variability becomes substantially weaker.

Thus, it may be necessary to incorporate additional mechanisms for increased ocean heat uptake when simulating the early Pliocene climate and, potentially, the response of the tropics to contemporary global warming. The enormous impacts of changes in the warm pool (such as shifts in global precipitation patterns and cloud cover), as well as tentative evidence that the tropical belt has been expanding poleward over the past few decades (31), make our findings especially relevant to current discussions about global warming.

References and Notes
1. J. Zachos, M. Pagani, L. Sloan, E. Thomas, K. Billups, *Science* **292**, 686 (2001).
2. G. H. Haug, R. Tiedemann, R. Zahn, A. C. Ravelo, *Geology* **29**, 207 (2001).

3. M. E. Raymo, B. Grant, M. Horowitz, G. H. Rau, *Mar. Micropaleontol.* **27**, 313 (1996).
4. H. Dowsett, J. Barron, R. Poore, *Mar. Micropaleontol.* **27**, 13 (1996).
5. A. M. Haywood, P. J. Valdes, B. W. Sellwood, *Global Planet. Change* **25**, 239 (2000).
6. A. V. Fedorov *et al.*, *Science* **312**, 1485 (2006).
7. M. W. Wara, A. C. Ravelo, M. L. Delaney, *Science* **309**, 758 (2005); published online 23 June 2005 (10.1126/science.1112596).
8. P. S. Dekens, A. C. Ravelo, M. D. McCarthy, *Paleoceanography* **22**, PA3211 (2007).
9. J. R. Marlow, C. B. Lange, G. Wefer, A. Rosell-Melé, *Science* **290**, 2288 (2000).
10. K. T. Lawrence, Z. Liu, T. D. Herbert, *Science* **312**, 79 (2006).
11. P. Molnar, M. A. Cane, *Paleoceanography* **17**, 1021 (2002).
12. A. V. Fedorov, S. G. Philander, *Science* **288**, 1997 (2000).
13. S. G. H. Philander, *El Niño, La Niña, and the Southern Oscillation* (Academic Press, New York, 1990).
14. A. M. Haywood, P. J. Valdes, V. L. Peck, *Paleoceanography* **22**, PA1213 (2007).
15. See supporting material on *Science* Online.
16. A. A. Velichko, I. Spasskaya, in *The Physical Geography of Northern Eurasia*, M. Shahgedanova, Ed. (Oxford Univ. Press, Oxford, 2002), pp. 36–69.
17. T. D. Herbert, J. D. Schuffert, *Proc. ODP Sci. Res.* **159T**, 17 (1998).
18. G. Bartoli *et al.*, *Earth Planet. Sci. Lett.* **237**, 33 (2005).
19. J. Tian, *Earth Planet. Sci. Lett.* **252**, 72 (2006).
20. G. H. Haug, D. M. Sigman, R. Tiedemann, T. F. Pedersen, M. Sarnthein, *Nature* **433**, 821 (2005).
21. J. Groeneveld *et al.*, *Proc. ODP Sci. Res.* **202**, 1 (2006).
22. H. J. Dowsett, M. M. Robinson, *Philos. Trans. R. Soc. London Ser. A* **367**, 109 (2009).
23. Data are available from http://geology.er.usgs.gov/eespteam/prism/prism_data.html.
24. A. C. Clement, R. Seager, G. Murtugudde, *J. Clim.* **18**, 5294 (2005).
25. M. Barreiro, G. Philander, R. Pacanowski, A. V. Fedorov, *Clim. Dyn.* **26**, 349 (2006).
26. J. Lu, G. A. Vecchi, T. Reichler, *Geophys. Res. Lett.* **34**, L06805 (2007).
27. U. Salzmann, A. M. Haywood, D. J. Lunt, P. J. Valdes, D. J. Hill, *Glob. Ecol. Biogeogr.* **17**, 432 (2008).
28. I. M. Held, B. J. Soden, *J. Clim.* **19**, 5686 (2006).
29. S. G. H. Philander, A. V. Fedorov, *Paleoceanography* **18**, 1045 (2003).
30. R. L. Sriver, M. Huber, *Nature* **447**, 577 (2007).
31. D. J. Seidel, Q. Fu, W. J. Randel, T. J. Reichler, *Nat. Geosci.* **1**, 21 (2008).
32. A.V.F. thanks G. Philander, M. Barreiro, R. Pacanowski, Y. Rosenthal, C. Ravelo, P. deMenocal, P. Dekens, A. Haywood, and C. Wunsch for numerous discussions of this topic. Supported by NSF grant OCE-0550439, U.S. Department of Energy Office of Science grants DE-FG02-06ER64238 and DE-FG02-08ER64590, and a David and Lucile Packard Foundation fellowship (A.V.F.), NSF grant OCE-0623487 (T.D.H.), and a Flint Fellowship at Yale University (Z.L.).

Structure of P-Glycoprotein Reveals a Molecular Basis for Poly-Specific Drug Binding

Stephen G. Aller,[1] Jodie Yu,[1] Andrew Ward,[2] Yue Weng,[1,4] Srinivas Chittaboina,[1] Rupeng Zhuo,[3] Patina M. Harrell,[3] Yenphuong T. Trinh,[3] Qinghai Zhang,[1] Ina L. Urbatsch,[3] Geoffrey Chang[1]†

P-glycoprotein (P-gp) detoxifies cells by exporting hundreds of chemically unrelated toxins but has been implicated in multidrug resistance (MDR) in the treatment of cancers. Substrate promiscuity is a hallmark of P-gp activity, thus a structural description of poly-specific drug-binding is important for the rational design of anticancer drugs and MDR inhibitors. The x-ray structure of apo P-gp at 3.8 angstroms reveals an internal cavity of ~6000 angstroms cubed with a 30 angstrom separation of the two nucleotide-binding domains. Two additional P-gp structures with cyclic peptide inhibitors demonstrate distinct drug-binding sites in the internal cavity capable of stereoselectivity that is based on hydrophobic and aromatic interactions. Apo and drug-bound P-gp structures have portals open to the cytoplasm and the inner leaflet of the lipid bilayer for drug entry. The inward-facing conformation represents an initial stage of the transport cycle that is competent for drug binding.

The American Cancer Society reported over 12 million new cancer cases and 7.6 million cancer deaths worldwide in 2007 (*1*). Many cancers fail to respond to chemotherapy by acquiring MDR, to which has been attributed the failure of treatment in over 90% of patients with metastatic cancer (*2*). Although MDR can have several causes, one major form of resistance to chemotherapy has been correlated with the pres-

ence of at least three molecular "pumps" that actively transport drugs out of the cell (*3*). The most prevalent of these MDR transporters is P-gp, a member of the adenosine triphosphate (ATP)–binding cassette (ABC) superfamily (*4*). P-gp has unusually broad poly-specificity, recognizing hundreds of compounds as small as 330 daltons up to 4000 daltons (*5*, *6*). Most P-gp substrates are hydrophobic and partition into the lipid bilayer (*7*, *8*). Thus, P-gp has been likened to a molecular "hydrophobic vacuum cleaner" (*9*), pulling substrates from the membrane and expelling them to promote MDR.

Although the structures of bacterial ABC importers and exporters have been established (*10–15*) and P-gp has been characterized at low resolution by electron microscopy (*16*, *17*), obtaining an x-ray structure of P-gp is of particular interest because of its clinical relevance. We describe the structure of mouse P-gp (ABCB1), which has 87% sequence

identity to human P-gp (fig. S1), in a drug-binding–competent state (*18*, *19*). We also determined cocrystal structures of P-gp in complex with two stereoisomers of cyclic hexapeptide inhibitors, cyclic-*tris*-(*R*)-valineselenazole (QZ59-RRR) and cyclic-*tris*-(*S*)-valineselenazole (QZ59-SSS), revealing a molecular basis for poly-specificity.

Mouse P-gp protein exhibited typical basal adenosine triphosphatase (ATPase) activity that was stimulated by drugs like verapamil and colchicine (fig. S2A) (*20*). P-gp recovered from washed crystals retained near-full ATPase activity (fig. S3). Both QZ59 compounds inhibited the verapamil-stimulated ATPase activity in a concentration-dependent manner (fig. S2B). Both stereoisomers inhibited calcein-AM export with median inhibitory concentration (IC_{50}) values in the low micromolar range (fig. S4) and increasing doses of QZ59 compounds resulted in greater colchicine sensitivity in P-gp–overexpressing cells (fig. S5).

The structure of P-gp (Fig. 1) represents a nucleotide-free inward-facing conformation arranged as two "halves" with pseudo two-fold molecular symmetry spanning ~136 Å perpendicular to and ~70 Å in the plane of the bilayer. The nucleotide-binding domains (NBDs) are separated by ~30 Å. The inward-facing conformation, formed from two bundles of six transmembrane helices (TMs 1 to 3, 6, 10, 11 and TMs 4, 5, 7 to 9, 12), results in a large internal cavity open to both the cytoplasm and the inner leaflet. The model was obtained as described in (*18*) by using experimental electron density maps (figs. S6 and S7 and table S1), verified by multiple $F_{obs} - F_{calc}$ maps (figs. S8 to S10), with the topology confirmed by (2-hydroxy-5-nitrophenyl)mercury(II) chloride (CMNP)–labeled cysteines (figs. S6, B to D; S7C, and S11, and table S2). Two portals (fig. S12) allow access for entry of hydrophobic molecules directly from the membrane. The portals are formed by TMs 4 and 6 and TMs 10 and 12, each of which have smaller side chains that could allow tight packing during NBD dimeriza-

[1]Department of Molecular Biology, The Scripps Research Institute, 10550 North Torrey Pines Road, CB105, La Jolla, CA 92037, USA. [2]Department of Cell Biology, The Scripps Research Institute, 10550 North Torrey Pines Road, CB105, La Jolla, CA 92037, USA. [3]Cell Biology and Biochemistry, Texas Tech University Health Sciences Center, 3601 4th Street, Lubbock, TX 79430, USA. [4]College of Chemistry and Molecular Sciences, Wuhan University, Wuhan, 430072 P. R. China.

†To whom correspondence should be addressed. E-mail: gchang@scripps.edu

Supporting Online Material for

Greatly Expanded Tropical Warm Pool and Weakened Hadley Circulation in the Early Pliocene

Chris M. Brierley, Alexey V. Fedorov,* Zhonghui Liu, Timothy D. Herbert, Kira T. Lawrence, Jonathan P. LaRiviere

*To whom correspondence should be addressed. E-mail: alexey.fedorov@yale.edu

This PDF file includes:

SOM Text

Figs. S1 to S3

Tables S1 to S3

References

Paleo Observations in Fig. 1: We generated about 900 alkenone SST measurements in this study, covering the time interval between ~1.8 Ma and ~4 Ma from ODP Site 1012 (32º17'N, 118º24'W). We sampled sediments every 15 cm for the interval 126-187 m and every 20 cm for the remaining core (187-282 m), for an average 3-kyr resolution. Pliocene SST changes at ODP 1012 were estimated based on the alkenone unsaturation index ($U^{K'}_{37}$), defined as $U^{K'}_{37}=C_{37:2}/(C_{37:2}+C_{37:3})$, where $C_{37:2}$ and $C_{37:3}$ are the concentrations of di- and tri-unsaturated C_{37} alkenones (*S1*). Reproducibility for $U^{K'}_{37}$ is better than ±0.005, corresponding to a temperature uncertainty of ± 0.15ºC using the calibration of Prahl et al. (*S1*). The Pliocene chronology at ODP 1012 is based on 5 biostratigraphic control points from the ODP initial report (*S2*), and further refined by correlating similar features in both this record and the SST record from ODP 846 (*10*). The newly generated Pliocene SST record from ODP 1012 was then combined with existing records from ODP 1012 (*S3*) and ODP 846 (*10*) to reconstruct the meridional SST gradient in the eastern Pacific.

Paleo Observations in Fig. 2: Fig. 2 combines currently available proxy SST data from Mg/Ca and alkenone techniques for the early Pliocene. Specifically for this paper we produced alkenone proxy temperatures for ODP sites 982, 1090, and DSDP 607 (in addition to ODP 1012) using the same methodology as described above. We also utilized results of previous studies *(6-10, 17-21)*. The chosen period of the reconstruction, around 4-4.2 Ma, coincides with the time when the east-west temperature gradient along the equator almost fully collapsed (*6,* fig. 1d) and is in the middle of the early Pliocene warm interval.

Our reconstruction of the meridional SST distribution in the open ocean in the Pacific (roughly along the dateline) invokes several temperature adjustments, because of scarcity of available temperature data. One important basis of these adjustments is that the data indicate very weak temperature variations, both zonal and meridional, within the tropical warm pool. For example, the maximum SST for this time interval is roughly 28.5ºC (in the equatorial region), while the temperature in the upwelling zone off the coast of California at 33ºN is 26ºC, so we can assume that the temperature in the middle of the Pacific at this particular latitude will lie between these two numbers, say 27ºC. Other important assumptions include the assumptions that modern differences between Atlantic and Pacific temperatures at given latitude persisted throughout the Pliocene and that the climate cooled between the early to mid-Pliocene by roughly 2ºC (which is consistent with available data). The detailed description of the adjustments is below:

(a) If a data point originates from a coastal or equatorial upwelling region, we add a correction of +1ºC, in order to estimate the temperature away from the coast. This correction is rather conservative. If tropical temperatures in the early Pliocene did not exceed 28-29ºC, as suggested by available data, the upper bound on this correction is 2-3ºC, which would raise our SST estimates at around 30ºN even higher.
(b) If a data point is from the northern Atlantic (to the north of 35ºN), we subtract 4ºC to allow for the difference between the Atlantic and Pacific. At present, surface waters in the North Pacific are generally 2 to 7ºC colder than in the Atlantic at the same latitude. The chosen correction (4ºC) gives a very good agreement at 50ºN where we have data both from the Pacific and the Atlantic.
(c) For the data point from the southern Atlantic (at 42ºS) we add 4ºC, which corresponds to the modern difference between this location in the Atlantic and the Pacific dateline temperature.

(d) For the data point from the northern Pacific (at 50ºN) we add 1ºC, which corresponds to the modern difference between this location and the dateline temperature.

(e) Finally, if a data set extends only to 3 Ma, we add 2ºC to allow for climate cooling between 4 to 3Ma, since most of the available data for the Pliocene exhibit a cooling trend of 1.5-2.5ºC for this time interval.

Although these corrections may introduce errors in some of our temperature estimates (we expect of the order of 1-2ºC), the overall temperature distribution, represented by the thick line in Fig. 2, is very robust and does not depend on any particular data point. Table S1 combines the original data and the appropriate adjustments.

The SST profile used in GCM simulations for the Pliocene: The SST profile used in boundary conditions for the atmospheric GCM has a generic exponential form with parameters chosen to fit the data in Fig. 2. The equation takes the form:

$$T(\theta) = (T_{max} - T_{min})\exp\left[\frac{1}{a}\left(\frac{|\theta|}{45}\right)^N\right] + T_{min} \qquad (1)$$

where θ is the latitude in degrees, T_{min} is the temperature of freezing for sea water (set to 1.8ºC). T_{max} is the maximum temperature in the tropics (set to 28.5ºC). N is set to 4.5; while constant a is determined by a least-squares fit to the temperature estimates in Fig. 2. The value of a differs in the Atlantic from the rest of globe to allow for warmer temperatures in the North Atlantic:

$$a = \begin{cases} 4.2 \Rightarrow \theta \geq 270, \phi \geq 0 \\ 2.6 \Rightarrow otherwise \end{cases} \qquad (2)$$

To replicate the annual cycle, the SST profile is shifted along the meridian seasonally to match the progression of the modern annual cycle.

To simulate the effect of the Peru Current along the coast of South America, which was warmer than at present but still colder than the surrounding waters (*8*), we add a cold temperature anomaly, T_{Peru}, to our SST profile:

$$T_{Peru} = \begin{cases} -3\cos^2\left[90\frac{\phi+65}{30}\right]\cos^2\left[90\frac{\theta+30}{30}\right] \Rightarrow -75 \leq \theta \leq 15, -110 \leq \phi \leq -65 \\ 0 \Rightarrow otherwise \end{cases} \qquad (3)$$

The SST tropical pattern given by equations (1-3) is shown in Figure S1.

Details of atmospheric GCM simulations: The model simulations were performed using the Community Atmosphere Model (CAM3, *S4*) developed by the National Center for Atmospheric Research (NCAR). It is a three-dimensional spectral model of global extent, with 26 vertical levels and a horizontal truncation of T42 (~2.8º transform grid). We use the model set-up as described by Hack et al. (*S5*). The model source code and the present-day climatogical boundary conditions are freely accessible on the Earth System Grid (www.earthsystemgrid.org).

The model has been spun up for 15 months, after which it has reached dynamic equilibrium. The simulations are then integrated for another decade – the results presented are the average of these final 10 years. The simulation of the modern climate has an atmospheric heat transport across the

equator (Fig. S2). Although this is a feature of the real climate system, it is exaggerated by the model's coarse meridional resolution near the equator.

For the early Pliocene run, we use the reconstructed SST profile as the surface boundary condition and also introduce several other modifications based on the PRISM reconstruction (*21*); including the removal of the Greenland ice sheet, a reduction in the height of the Rockies, Andes and Indonesia to their suggested early Pliocene altitudes, and changes in the Arctic vegetation. A fractional sea ice cover was introduced between the seawater freezing point (T_{min}) and 0ºC. Sensitivity studies have shown that the impact of the imposed SST profile on the Hadley circulation is an order of magnitude larger than the impact of other model modifications (Table S2).

The radiative fluxes quoted in the main body of the paper are derived from the top-of-atmosphere (TOA) fluxes diagnosed by the model and the surface temperatures. The TOA fluxes are divided into clear-sky net longwave, clear-sky net shortwave and cloudy net flux. The radiative response to the increased surface temperatures is calculated assuming blackbody radiation. The water vapour response is computed as the residual of the clear-sky longwave minus the increase blackbody radiation. Inclusion of a more realistic longwave emissivity does not significantly alter the proportions of warming explained by water vapor and cloud feedbacks.

Atmospheric CO_2 concentrations measured in 1990 (355ppm) are used for both Pliocene and present-day simulations (*3*). The atmospheric and oceanic contributions to the heat transport implied by the model are calculated by evaluating heat fluxes at the top of the atmosphere and at the ocean surface (Fig. S3).

Details of coupled GCM simulations: The coupled simulations were performed using the third version of NCAR's Community Climate System Model (CCSM3). This GCM incorporates the atmospheric component described above (CAM3) coupled to ocean and sea ice models (POP and CSIM, respectively). CCSM3 has been used extensively for climate simulations which contributed, for example, to the IPCC Fourth Assessment Report (*S6*). A comprehensive description of the model can be found in Collins *et al.* (*S7*). The model source code and the boundary conditions are freely accessible on the Earth System Grid (www.earthsystemgrid.org).

The experiments discussed in this paper start from an equilibrated preindustrial climate. Two runs are initialized with an instantaneous increase of atmospheric CO_2 concentrations to 355ppm (the level of 1990). The first run uses the standard model set-up, whilst the other has ocean background vertical diffusivity (increased by a factor of 10 in the top 400m, between 40ºS and 40ºN). Both runs have been spun-up for 120 years, and an average of the last 20 years is chosen to make the comparison in Fig. 5.
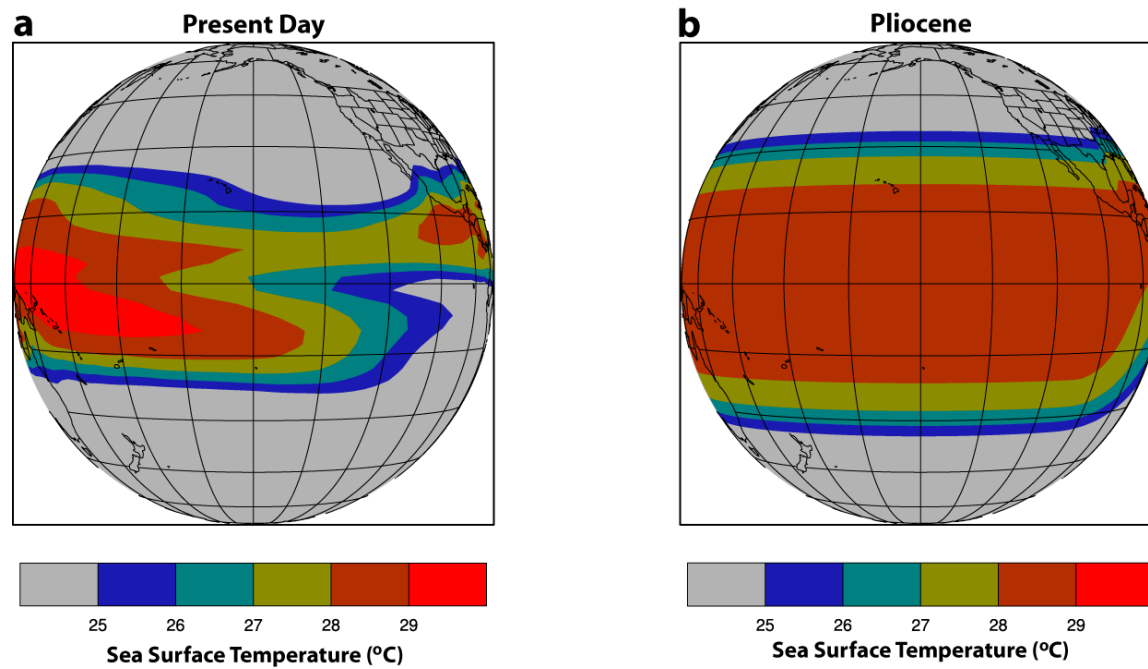
Figures (Supplementary Online Material)

Figure S1. Patterns of mean tropical SSTs showing the extent of the ocean warm pool for the present and early Pliocene climates. The idealized Pliocene SSTs are based on equations (1-3) and the data in Fig. 2.
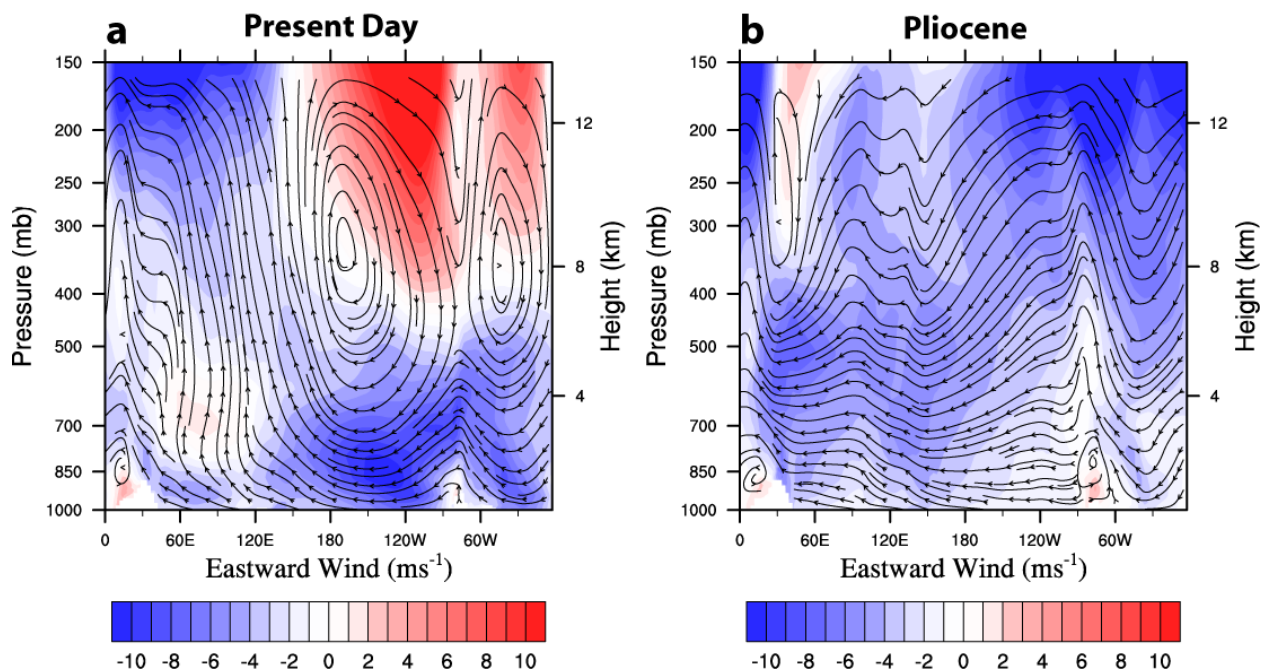
Figure S2. The equatorial circulation in the atmospheric GCM for (a) the present climate and (b) the early Pliocene climate. Instantaneous flow streamlines and the strength of zonal winds (in m/s) in the equatorial plane are shown. Vertical motion has been scaled by a factor of 10^3, so it would appear of the same magnitude as the horizontal motion. The Walker Circulation, evident in the left panel between 150°E and 80°W, is absent in the Pliocene simulation. There is also a corresponding weakening of the low level easterly winds over the equatorial Pacific (from roughly 10 ms^{-1} to 2 ms^{-1}).
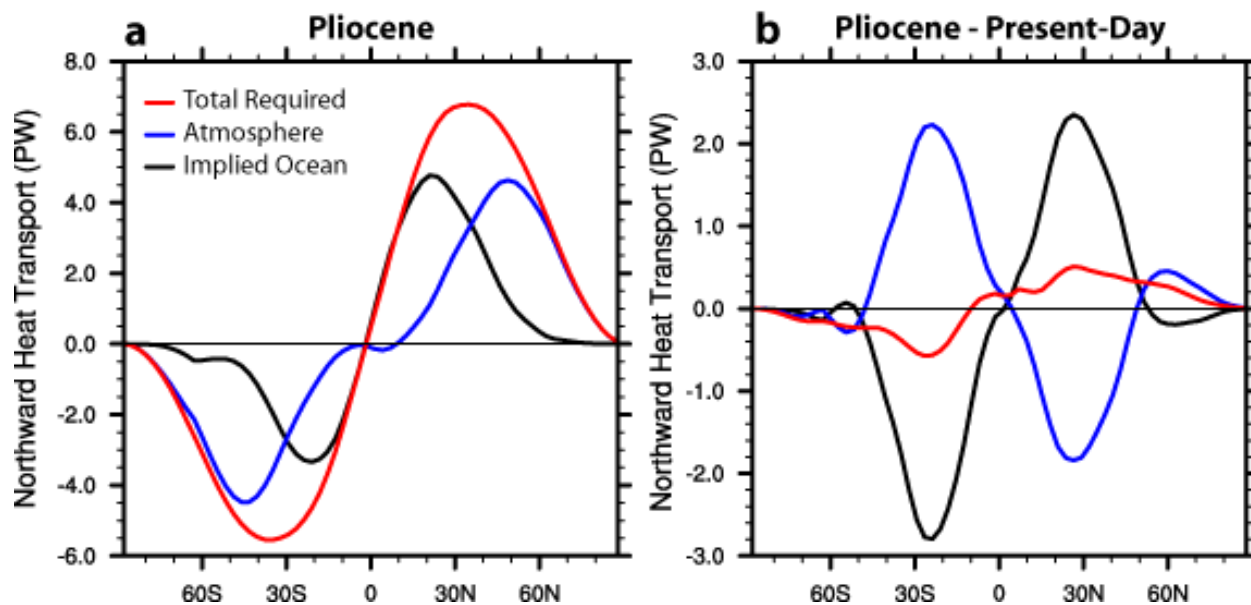
Figure S3. (a) The poleward heat transports simulated in the Pliocene experiment by the atmospheric GCM. Red line: total poleward heat transport. Blue line: atmospheric transport. Black line: implied oceanic heat transport. (b) Differences in these transports between the Pliocene and the present-day climate (shown with the same line colors). For the early Pliocene, the calculations show a slight increase in total poleward heat transport and a strong increase in implied oceanic heat transport.

Reference	Method	Site	Location	Lat.	Lon.	Averaging Interval	Local SST for interval (°C)	Temporal correction (°C)	Location correction (°C)	Est. SST (°C) for the mid-
Atlantic:										
Herbert and Schuffert 1998	Alken.	ODP 958A	NW African margin	23°N	20°W	4-4.3Ma	26.5		+1	27.5
This study	Alken.	DSDP 607	N Atlantic	41°N	33°W	3.9-4.1Ma	21.5		-4	17.5
Bartoli et al. 2005	Mg/Ca	DSDP 609	N Atlantic	50°N	24°W	2.8-3.3Ma	15	+2	-4	13
This study	Alken.	ODP 982	N Atlantic	58°N	16°W	3.9-4.1Ma	17.5		-4	13.5
Bartoli et al. 2005	Mg/Ca	ODP 984	N Atlantic	61°N	24°W	2.8-3.1Ma	10	+2	-4	8
Marlow et al. 2000	Alken.	ODP 1084	SW African margin	26°S	13°E	4-4.3Ma	26.5		+1	27.5
This study	Alken.	ODP 1090	S Atlantic	42°S	8°E	2.5-3.1Ma	13.5	+2	+4	19.5
Pacific:										
Fedorov et al. 2006	Alken	ODP 847	E Eq Pacific	0°	95°W	4-4.3Ma	28			28
Wara et al. 2005	Mg/Ca	ODP 847	E Eq Pacific	0°	95°W	4-4.3Ma	28			28
Wara et al. 2005	Mg/Ca	ODP 806	W Eq Pacific	0°	159°E	4-4.3Ma	28			28
Lawrence et al. 2006	Alken.	ODP 846	E Eq Pacific	3°S	91°W	4-4.3Ma	27		+1	28
Groeneveld et al. 2006, calibrated by Dekens et al. 2007	Mg/Ca	ODP 1241	E Eq Pacific	3°N	88°W	4-4.3Ma	28.5			28.5
Tian et al. 2006	Mg/Ca	ODP 1143	S China Sea	9°N	113°E	3.1-3.3Ma	28.5			28.5
This study	Alken.	ODP 1012	Calif margin	32°N	118°W	3.9-4.1Ma	24.5		+1	25.5
Fedorov et al. 2006, Dekens et al. 2007	Alken.	ODP 1014	Calif margin	33°N	120°W	4-4.3Ma	25		+1	26
Haug et al. 2005	Alken.	ODP 882	N Pacific	50°N	167°E	2.8-3.2Ma	10.5	+2	+1	13.5
Indian:										
Dekens 2007 (PhD thesis)	Mg/Ca	ODP 758	Indian	5°N	90°E	3-5Ma	27.5			27.5

Table S1: SST estimates used in reconstructing the meridional temperature distribution in the Pacific during the early Pliocene (Fig. 2), including references, methods, site locations, and temperature corrections when appropriate.

	Strength of Northern Hadley Cell (10^{10} kg/s)	Strength of Southern Hadley Cell (10^{10} kg/s)
Present-day run (Control)	7.0	9.6
Early Pliocene:		
Standard run (10-year duration)	5.0	4.4
A longer spin-up time (20-year duration)	4.9	4.4
Pliocene SSTs, other surface boundary conditions (e.g. orography, land surface, and ice sheets) as Present-day	5.0	4.5
0.5^{o}C zonal SST gradient imposed along the equator	4.9	4.7
Maximum SST increased to 29°C	5.0	4.5
Pliocene SST profile with slightly altered coefficients in eq. (1) giving faster decrease in SST with latitude (a=2.5, N=4)	5.3	4.8
Tropical Pliocene SSTs merged (between 40° and 60° latitude) with present-day SSTs in high latitudes	5.4	4.6

Table S2: The sensitivity of the strength of the Hadley circulation to changes in the surface boundary conditions. The results show that the reduction in the Hadley Cell intensity is a robust feature of the Pliocene simulations (caused by the strong reduction in the meridional SST gradient).

Location	Present Obs.	Pliocene Paleodata	Present CAM3	Pliocene CAM3	PRISM CAM3	PRISM HadAM3
West Coast USA	459±67	693±300	617±306	536±190	625±249	967±364
East Cost USA	1030	1280	1050	864	1311	676
N. Mediterranean	772±300	1163±110	580±165	647±120	1227±754	830±422
S. Mediterranean	369±28	468±90	91±82	244±136	428±391	418±122
East Africa	692	1000	765	1375	1479	700
China, Shanxi	482	800	1034	1125	1073	1533
China, Yunnan	1389±637	1083±13	1054	1149	1182	1563
NE Australia	1177	2075±601	1097	1643	1178	1075
SE Australia	618±254	2100±458	493±234	768±168	497±159	861±393

Table S3: Comparison of the modelled mean annual precipitation (mm/yr) in several regions to terrestrial paleo-reconstructions. The paleodata, present-day observations and PRISM HadAM3 columns are taken from Table 2 of Salzmann et al. (*25*). The paleodata comes from a variety sources based on palynological inferences (for discussion and references see *25*). The four rightmost columns present the mean annual precipitation as diagnosed using different atmospheric models. "Pliocene CAM3" and "Present CAM3" are the early Pliocene reconstruction and modern control run presented in this work and use version 3 of the Community Atmosphere Model (*S4*). "PRISM CAM3" uses the Pliocene Research, Interpretation and Synoptic Mapping (PRISM) paleoenvironmental reconstruction for the mid-Pliocene (*S8*) as the boundary conditions for a simulation with CAM3. PRISM HadAM3 refers to an atmospheric GCM run (performed by Haywood and Valdes, *S9*) using the 3rd version of the Hadley Centre's Atmosphere Model and incorporating the Mid-Pliocene boundary conditions of Dowsett et al. (*S8*). Differences between the final two columns can be interpreted, in part, as the uncertainty caused by differences in the atmospheric models. The error bars quoted indicate the standard deviation between the individual locations incorporated in the regional average. Note the large uncertainties both in paleo-observations and model simulation. Our Pliocene simulation is also consistent with other qualitative precipitation paleo-observations (*S10*, *S11*)

Supporting Online Material References:

S1.   F. G. Prahl, L. A. Muehlhausen, D. L. Zahnle, *Geochim. Cosmochim. Acta* **52**, 2303 (1988).

S2.   Shipboard Scientific Party, Site 1012, *Proc. ODP, Init. Repts.* **167**, 129 (1997).

S3.   Z. Liu, M. A. Altabet, T. D. Herbert, *Geophys. Res. Lett.* **32**, L23607 (2005).

S4.   W. D. Collins *et al., J. Clim.* **19**, 2144 (2006).

S5.   J. J. Hack *et al.*, *J. Clim.***19**, 2267 (2006).

S6.   D. Randall et al., in *Climate Change 2007: The Physical Science Basis*, S. Solomon et al. (Cambridge University Press, 2007)

S7.   W. D. Collins *et al., J. Clim.* **19**, 2122 (2006).

S8.   H. J. Dowsett, M. A. Chandler, T. M. Cronin, G. S. Dwyer, *Paleoceanography* **20**, PA2014 (2005). An updated version of this dataset is now available (*21*), however we used the old version to allow comparison to previously published results (*25*).

S9.   A. M. Haywood, P. J. Valdes, *Palaeogeogr. Palaeocl.* **237**, 412 (2006)

S10.   P. deMenocal, *Earth. Planet. Sc. Lett.* **220**, 3 (2004)

S11.   L. M. Dupont, B. Donner, L. Vidal, E. M. Pérez, G. Wefer, *Geology* **33,** 461 (2005)